Inorg. Chem. **2005**, *44*, 6228–6239

Large M_4L_4 (M = Al(III), Ga(III), In(III), Ti(IV)) Tetrahedral Coordination Cages: an Extension of Symmetry-Based Design

Robert M. Yeh, Jide Xu, Georg Seeber, and Kenneth N. Raymond*

Department of Chemistry, University of California, Berkeley, California 94720-1460

Received April 5, 2005

As an extension to a rational design for the formation of self-assembled coordination cages, the syntheses for very large M_4L_4 tetrahedra based on a hexadentate 3-fold symmetric ligand (1,3,5-tris(4′-(2″,3″-dihydroxybenzamido)-phenyl)benzene ($H_6\mathbf{L}^2$)) are described. Four tetrahedral $M_4\mathbf{L}^2{}_4$ assemblies (M = Al(III), Ga(III), In(III), Ti(IV)), with cavity sizes of around 450 Å^3, have been characterized by elemental analysis, NMR spectroscopy, and high-resolution electrospray mass spectrometry. Differences in chiral resolution and dynamic behavior of host–guest interactions with previously reported tetrahedral $M_4\mathbf{L}^N{}_6$ and $M_4\mathbf{L}^1{}_4$ architectures are highlighted for the ligands 1,5-bis(2′,3′-dihydroxybenzamido)naphthalene ($H_4\mathbf{L}^N$) and 1,3,5-tris(2′,3′-dihydroxybenzamido)benzene ($H_6\mathbf{L}^1$). An even larger 3-fold symmetric ligand, 1,3,5-tris(4′-(2‴,3‴-dihydroxybenzamido)-1′,1″-biphenyl)benzene ($H_6\mathbf{L}^3$) has been prepared but, due to increased flexibility and deviation from the intended 3-fold symmetry, does not undergo self-assembly to form the $M_4\mathbf{L}^3{}_4$ structure.

Introduction

The design and synthesis of functional materials via self-assembly of molecular components is an important aspect of the "bottom-up" approach to nanotechnology. In particular, self-assembled supramolecular host species that incorporate cavities of various shapes and sizes have proven application in areas such as catalytic host−guest chemistry.[1−9] In several recent examples, such supramolecular entities consist of discrete metal−ligand coordination assemblies with functions that are unattainable within the constituent molecular components per se.[10−17] In the many reports of cavity-containing coordination assemblies, most display host−guest chemistry that is limited to encapsulation of small ions or solvent molecules.[18−20] Nevertheless, versatile metal−ligand coordination hosts with a rich repertoire of host−guest chemistry do exist. For example, a number of palladium−pyridyl cages have been shown to encapsulate multiple guest molecules and in some cases catalyze bimolecular reactions by virtue of confinement.[10−13]

A second, fundamental motivation for synthesizing new coordination host assemblies is to improve the understanding of the self-assembly process by probing the limits of "rational design" with larger and more complex structures. We have previously reported an $M_4\mathbf{L}^N{}_6$ tetrahedron (1,5-bis(2′,3′-

* To whom correspondence should be addressed. E-mail: raymond@socrates.berkeley.edu.

(1) Kang, J. M.; Rebek, J. *Nature* **1997**, *385*, 50−52.
(2) Hof, F.; Rebek, J. *Proc. Natl. Acad. Sci. U.S.A.* **2002**, *99*, 4775−4777.
(3) Diederich, F.; Felber, B. *Proc. Natl. Acad. Sci. U.S.A.* **2002**, *99*, 4778−4781.
(4) Slagt, V. F.; Reek, J. N. H.; Kamer, P. C. J.; van Leeuwen, P. *Angew. Chem., Int. Ed.* **2001**, *40*, 4271−4274.
(5) Stoddart, J. F.; Tseng, H. R. *Proc. Natl. Acad. Sci. U.S.A.* **2002**, *99*, 4797−4800.
(6) Rebek, J. *Acc. Chem. Res.* **1999**, *32*, 278−286.
(7) Kang, J. M.; Santamaria, J.; Hilmersson, G.; Rebek, J. *J. Am. Chem. Soc.* **1998**, *120*, 7389−7390.
(8) Kang, J. M.; Hilmersson, G.; Santamaria, J.; Rebek, J. *J. Am. Chem. Soc.* **1998**, *120*, 3650−3656.
(9) Karakhanov, E. E.; Maksimov, A. L.; Runova, E. A.; Kardasheva, Y. S.; Terenina, M. V.; Buchneva, T. S.; Guchkova, A. Y. *Macromol. Symp.* **2003**, *204*, 159−173.
(10) Kusukawa, T.; Nakai, T.; Okano, T.; Fujita, M. *Chem. Lett.* **2003**, *32*, 284−285.
(11) Ito, H.; Kusukawa, T.; Fujita, M. *Chem. Lett.* **2000**, 598−599.
(12) Yoshizawa, M.; Takeyama, Y.; Kusukawa, T.; Fujita, M. *Angew. Chem., Int. Ed.* **2002**, *41*, 1347−1349.
(13) Yoshizawa, M.; Kusukawa, T.; Fujita, M.; Sakamoto, S.; Yamaguchi, K. *J. Am. Chem. Soc.* **2001**, *123*, 10454−10459.
(14) Fiedler, D.; Pagliero, D.; Brumaghim, J. L.; Bergman, R. G.; Raymond, K. N. *Inorg. Chem.* **2004**, *43*, 846−848.
(15) Fiedler, D.; Leung, D. H.; Bergman, R. G.; Raymond, K. N. *J. Am. Chem. Soc.* **2004**, *126*, 3674−3675.
(16) Leung, D. H.; Fiedler, D.; Bergman, R. G.; Raymond, K. N. *Angew. Chem., Int. Ed.* **2004**, *43*, 963−966.
(17) Fiedler, D.; Bergman, R. G.; Raymond, K. N. *Angew. Chem., Int. Ed.* **2004**, *43*, 6748−6751.
(18) Swiegers, G. F.; Malefetse, T. J. *Chem. Rev.* **2000**, *100*, 3483−3537.
(19) Swiegers, G. F.; Malefetse, T. J. *Coord. Chem. Rev.* **2002**, *225*, 91−121.
(20) Leininger, S.; Olenyuk, B.; Stang, P. J. *Chem. Rev.* **2000**, *100*, 853−907.

10.1021/ic0505145 CCC: $30.25
Published on Web 08/05/2005

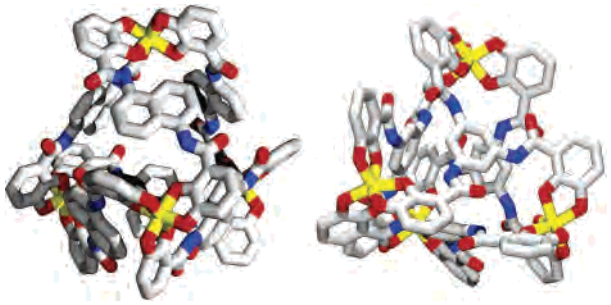

Figure 1. (left) The crystal structure of a "edge-on" tetrahedron $[Ga_4\mathbf{L}^N{}_6]^{12-}$ ($\mathbf{L}^N$ = 1,5-catecholatoamidonaphthalene) is shown (M−M distance 12.9 Å). (right) The crystal structure of $[Ti_4\mathbf{L}^1{}_4]^{8-}$ (M−M distance 11.5 Å). Although the M−M distance in this tetrahedral $M_4\mathbf{L}^1{}_4$ cluster is only 1.4 Å shorter than the M−M distance in the $M_4\mathbf{L}^N{}_6$ cluster shown on the left, the cavity of the $M_4\mathbf{L}^1{}_4$ cluster (≈40 Å^3) is 10 times smaller than the cavity of the $M_4\mathbf{L}^N{}_6$ cluster (≈450 Å^3). The interior of the $M_4\mathbf{L}^1{}_4$ structure appears to be more accessible because of bigger gaps between the ligands.

dihydroxybenzamido)naphthalene ($H_4\mathbf{L}^N$)) that exhibits varied host−guest chemistry within a cavity of approximately 450 Å^3, and it has recently been shown to enable enantio- and stereoselective catalysis.[15−17] This supramolecular host discriminates potential guest molecules on the basis of many physical factors including charge, hydrophobicity, size, and shape.[21,22] The original synthesis of this supramolecular cluster was based on a symmetry model which provided a rational basis for predicting the product of self-assembly.[23] In this M_4L_6 design, four pseudo-octahedral metal centers (tetrahedron vertices) are bridged by six 2-fold symmetric, bis-bidentate ligands (tetrahedron edges) in a M_4L_6 "edge-on" design (Figure 1),

We report here an extension of a different design strategy for a coordination tetrahedron. One of the goals is to create a new host assembly that offers a similar cavity size but a different cavity shape and accessibility than the previously described $M_4\mathbf{L}^N{}_6$ tetrahedron and thereby allow opportunities for new host−guest interactions. This alternative approach of tetrahedron formation combines four pseudo-octahedral metal centers (tetrahedron vertices) with four 3-fold symmetric, tris-bidentate ligands that cap the faces of the tetrahedron in a M_4L_4 "face-on" design (Figure 1).

There are a few precedents for M_4L_4 tetrahedral coordination assemblies based on the "face-on" approach.[24−26] In each case, the coordination assembly is formed from 3-fold symmetric ligands positioned on the faces of the tetrahedron and metal ions located at the four vertices. The largest of these M_4L_4 tetrahedra has a metal-to-metal distance of around 17 Å and resembles an open wire cage structure with a cavity that contains four *N*,*N*′-dimethylformamide solvent molecules in the solid state.[25] Many other examples of pseudo-3-fold-symmetric ligands do not generate the M_4L_4 tetrahedral structure.[27,28] Instead, other architectures, such as infinite networks, with varying metal−ligand stoichiometries are obtained, reflecting the different possible combinations of coordination number and geometry of both ligands and metal ions.

We reported some time ago small $M_4\mathbf{L}^1{}_4$ tetrahedra (M = Al^{III}, Ga^{III}, Fe^{III}, Ti^{IV}, and Sn^{IV}; 1,3,5-tris(2′,3′-dihydroxybenzamido)benzene ($H_6\mathbf{L}^1$)) based on this alternative design in which 3-fold symmetry of the ligand is achieved through 1,3,5-substitution of a benzene ring with catecholate chelators (Figure 1).[26] The 3-fold-symmetric, tris-bidentate ligands were combined with pseudo-octahedral metal centers, each coordinated by three bidentate chelators, to form tetrahedral clusters of the stoichiometry M_4L_4. These small $M_4\mathbf{L}^1{}_4$ clusters have a cavity size on the order of an ammonium (NH_4^+) cation, or approximately 40 Å^3. This paper describes the extension of the M_4L_4 design to the formation of much larger M_4L_4 tetrahedra with increased cavity capacity and hence promise for significant host−guest chemistry.

Results and Discussion

Design of M_4L_4 Tetrahedral Assemblies. The design of M_4L_4 tetrahedral assemblies can be simplified to designing rigid 3-fold-symmetric ligands that position the three chelate vectors within each ligand correctly for cluster formation.[26] Addition of a stoichiometric amount of the ligand and suitable six-coordinate metal ions then leads to the self-assembly of the M_4L_4 assembly. The importance of rigidity and planarity of the spacer between the chelating groups is highlighted in Figure 2, where two examples of quasi-3-fold-symmetric tris-catecholate ligands differ by only one methylene linker group between the chelators and the central scaffold.[26,29,30] The flexibility introduced by the methylene bridge results in the formation of the thermodynamically more stable mononuclear M_1L_1 metal complex. In contrast, the rigid, planar ligand forms the $M_4\mathbf{L}^1{}_4$ assembly which represents the lowest stoichiometric ratio of metal to ligand that can simultaneously satisfy the coordination number and geometry requirements of both the metal ion and ligand.

Analysis of the geometric relationship in the M_4L_4 tetrahedron assumes that each bidentate chelator on the ligand is planar. The angle between the ligand plane and the C_3 axis of the respective six-coordinate metal ion reveals an ideal approach angle of 19.4° that is required for the formation of the tetrahedron (Figure 2, definition of approach angles and their relationship to twist angles has been described in detail earlier).[22,31] This approach angle corre-

(21) Parac, T. N.; Caulder, D. L.; Raymond, K. N. *J. Am. Chem. Soc.* **1998**, *120*, 8003−8004.
(22) Caulder, D. L.; Raymond, K. N. *Dalton Trans.* **1999**, 1185−1200.
(23) Caulder, D. L.; Powers, R. E.; Parac, T. N.; Raymond, K. N. *Angew. Chem., Int. Ed.* **1998**, *37*, 1840−1843.
(24) Amoroso, A. J.; Jeffery, J. C.; Jones, P. L.; McCleverty, J. A.; Thornton, P.; Ward, M. D. *Angew. Chem. Int. Ed. Engl.* **1995**, *34*, 1443−1446.
(25) Albrecht, M.; Janser, I.; Meyer, S.; Weis, P.; Frohlich, R. *Chem. Commun.* **2003**, 2854−2855.
(26) Brückner, C.; Powers, R. E.; Raymond, K. N. *Angew. Chem., Int. Ed.* **1998**, *37*, 1837−1839.
(27) Fujita, M.; Umemoto, K.; Yoshizawa, M.; Fujita, N.; Kusukawa, T.; Biradha, K. *Chem. Commun.* **2001**, 509−518.
(28) Rosi, N. L.; Eddaoudi, M.; Kim, J.; O'Keeffe, M.; Yaghi, O. M. *Cryst. Eng. Commun.* **2002**, 401−404.
(29) Weitl, F. L.; Raymond, K. N. *J. Am. Chem. Soc.* **1979**, *101*, 2728−2731.
(30) Venuti, M. C.; Rastetter, W. H.; Neilands, J. B. *J. Med. Chem.* **1979**, *22*, 123−124.
(31) Caulder, D. L.; Brückner, C.; Powers, R. E.; Konig, S.; Parac, T. N.; Leary, J. A.; Raymond, K. N. *J. Am. Chem. Soc.* **2001**, *123*, 8923−8938.

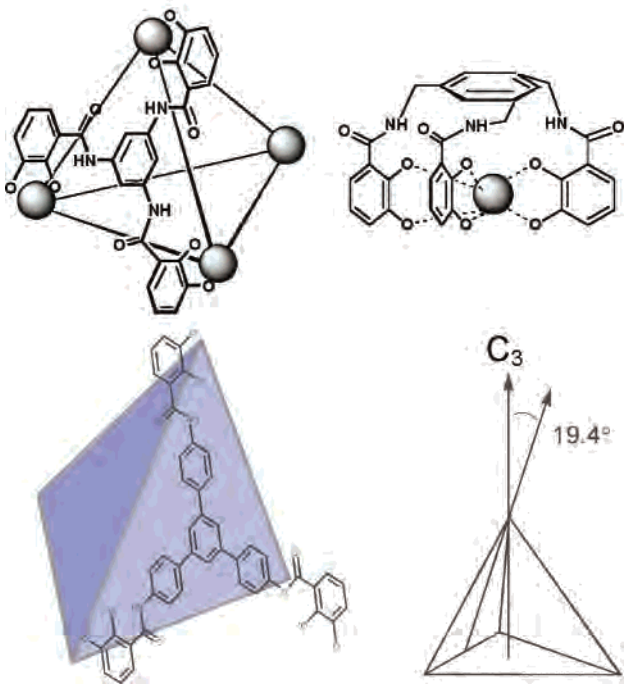

Figure 2. (top) The rigid 3-fold symmetric ligand on the left forms an $M_4\mathbf{L}^1{}_4$ tetrahedron, while the addition of methylene bridges to the ligand on the right adds sufficient flexibility to favor the formation of the mononuclear metal complex as the lowest stoichiometry product. (bottom) In the M_4L_4 "face-on" design (illustrated using $\mathbf{L}^2$), the 3-fold symmetric ligands are positioned on the faces of the tetrahedron. The angle between a vector in the plane of a face and the C_3 axis of a tetrahedron is 19.4°. This angle corresponds to the "approach angle" that the ligand chelators must adopt when coordinating to the metal ions on the vertexes.

sponds to a metal ion twist angle of 33.4° (the projection of the top trigonal face of the MO_6 polyhedron onto the bottom face). Titanium(IV) tris-catecholates have been found to have average twist angle of 35°, whereas Al(III), Ga(III), and Fe(III) tris-catecholates have average twist angles of 45°.[32] Therefore, tetravalent titanium ions are more suitable for the M_4L_4 structure than trivalent aluminum, gallium, and ferric ions. Nevertheless, because the phenylene-bridged ligand $H_6\mathbf{L}^2$ can distort from planarity, it is possible to accommodate both trivalent and tetravalent metal ions within the $M_4\mathbf{L}^2{}_4$ framework using the same ligand. Starting from the 1,3,5-tris-substituted benzene scaffold in $H_6\mathbf{L}^1$, two large 3-fold-symmetric ligands with rigid phenylene ($H_6\mathbf{L}^2$) and biphenylene linkers ($H_6\mathbf{L}^3$) (Scheme 1) were prepared.

Ligand Synthesis. The synthesis of $H_6\mathbf{L}^2$ begins with the synthesis of the intermediate 1,3,5-tris(4′-nitrophenyl)benzene. According to literature procedures, 4-nitroacetophenone reacts in the presence of ethanol and tetrachlorosilane through a double Aldol addition followed by an intramolecular condensation to yield 1,3,5-tris(4′-nitrophenyl)benzene.[33,34] While the cyclization reaction worked well for 4-bromoacetophenone as a substrate to form 1,3,5-tris(4′-bromophenyl)-benzene, 4-nitroacetophenone failed to yield the respective

Scheme 1

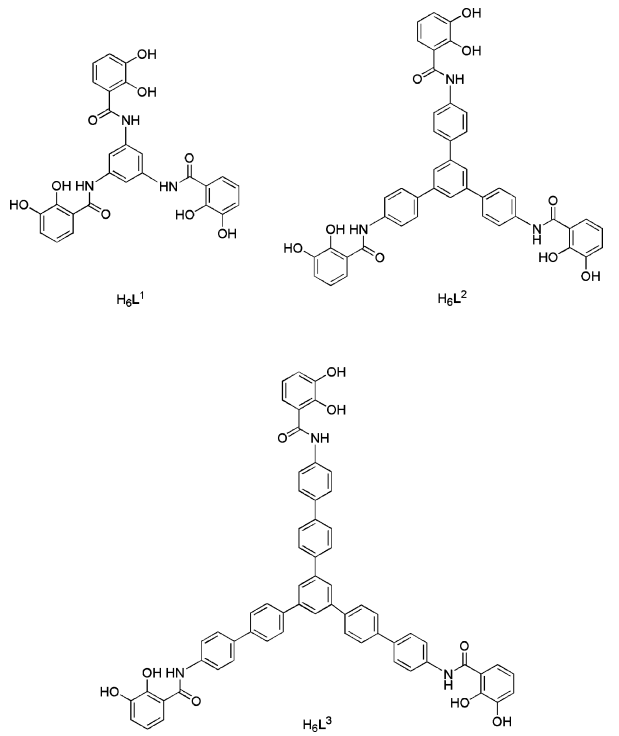

trimeric product. Furthermore, reactions of 4-nitroacetophenone in the presence of several other Lewis acid catalysts also failed to yield the trimerized product. Finally, under harsh reaction conditions, 1,3,5-tris(4′-nitrophenyl)benzene was synthesized from molten 4-nitroacetophenone in the presence of concentrated sulfuric acid and dry potassium pyrosulfate. Reduction of the three nitro groups to amino groups followed by amide-coupling with 2,3-dibenzyloxybenzoic acid chloride proceeded in acceptable yield to produce the benzyl-protected ligand $Bn_6\mathbf{L}^2$. Due to the low solubility of the protected ligand in common organic solvents, boron tribromide was used under heterogeneous conditions to cleave the protecting groups and provide the target ligand $H_6\mathbf{L}^2$.

A higher-yielding synthesis of the ligand $H_6\mathbf{L}^2$ was developed subsequently. Instead of a triple amide coupling reaction of 2,3-dibenzyloxybenzoic acid chloride to the 1,3,5-tris(4′-aminophenyl)benzene core, a palladium-catalyzed cross-coupling protocol was utilized. This reaction relies on a methyl-protected catecholamide−phenyl boronic ester. A very efficient triple Suzuki−Miyaura cross-coupling reaction of the methyl-protected boronic ester to 1,3,5-tribromobenzene was carried out under basic conditions with tetrakis-(triphenylphoshine)palladium as a catalyst. The methyl-protected ligand $Me_6\mathbf{L}^2$ was produced in 90% yield from the cross-coupling reaction. Heterogeneous deprotection with boron tribromide yielded the target ligand $H_6\mathbf{L}^2$ (Scheme 2).

The biphenylene extended ligand $H_6\mathbf{L}^3$ was synthesized using a convergent strategy (Scheme 2) also based on a triple Suzuki−Miyaura cross-coupling reaction. The central 1,3,5-tris(4′-bromophenyl)benzene core was prepared by condensation and cyclization of 4-bromoacetophenone following literature procedures.[33] Triple cross-coupling of the tribro-

(32) Davis, A. V.; Raymond K. N. *J. Am. Chem. Soc.,* in press.
(33) Elmorsy, S. S.; Pelter, A.; Smith, K. *Tetrahedron Lett.* **1991**, *32*, 4175−4176.
(34) Elmorsy, S. S.; Pelter, A.; Smith, K.; Hursthouse, M. B.; Ando, D. *Tetrahedron Lett.* **1992**, *33*, 821−824.

Scheme 2

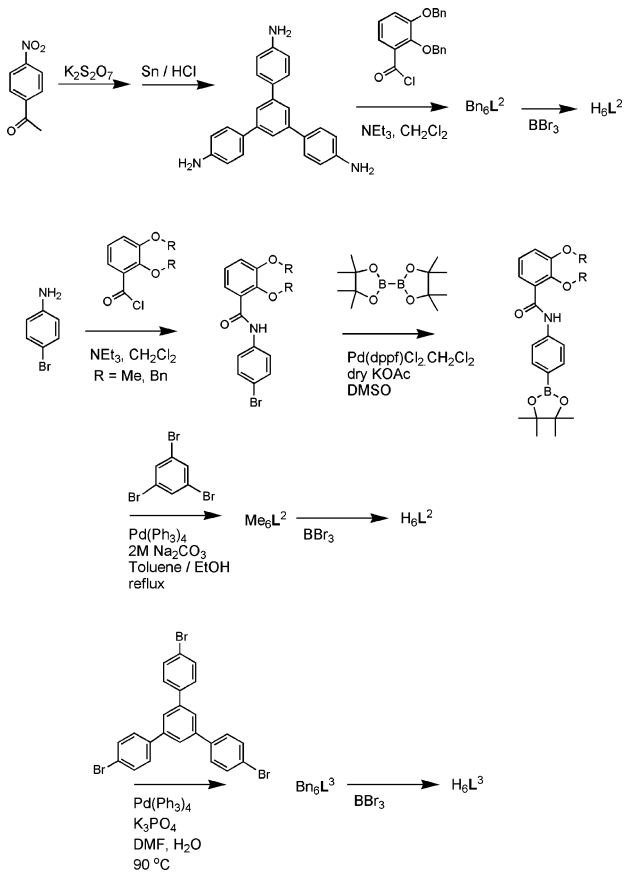

minated core with the benzyl-protected catecholamide−phenyl boronic ester, followed by BBr_3 deprotection, provided the ligand $H_6\mathbf{L}^3$.

Molecular Modeling. In our experience, molecular modeling has been a powerful tool for predicting coordination cage properties such as cavity shape, volume, accessibility, and hydrophobicity. The modeling protocol used has been successful at calculating the structures of three catecholate-based M_4L_6 tetrahedra and one catecholate-based M_4L_4 tetrahedron, all of which were later verified by X-ray crystallography.[23,26,31,35,36] The model for $M_4\mathbf{L}^2_4$ was built around four metal centers with identical chirality, and the starting coordinates of the metal tris-catecholates were based on the reported crystal structure of the small $M_4\mathbf{L}^1_4$ tetrahedral cluster.[26] Energy minimization was performed using MM3 force field calculations.[37] The first coordination sphere around each metal center and the dihedral angle between the catecholate planes and the amide groups were constrained. In this way, the only variables in the model are the metal-to-metal distances, with each metal−tris-catecholate moiety moving as a conserved unit during energy minimization, and the relative orientation of the rings within each ligand backbone.

The idealized tetrahedron model (Figure 3) is based on the $[Ga_4\mathbf{L}^2_4]^{12-}$ cluster that is a representative model for this

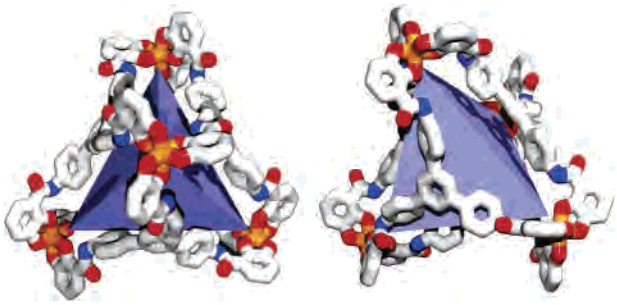

Figure 3. The cavity shape of the M_4L_4 cluster can be best approximated as a tetrahedron. Here are views down the vertex (left) and a face (right) showing an inscribed tetrahedron in the host cavity.

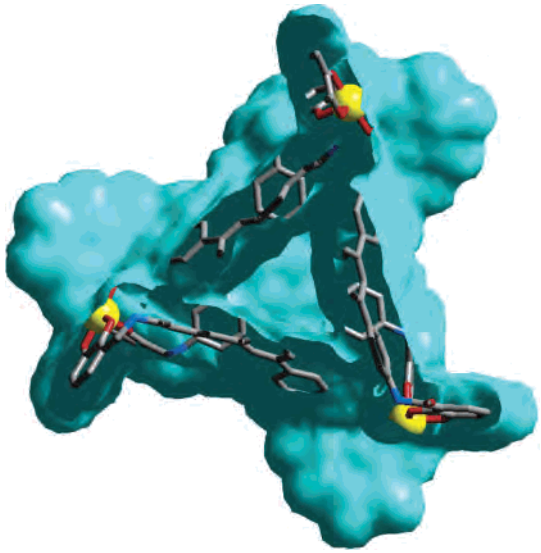

Figure 4. A view of the $[Ga_4L^2_4]^{12-}$ tetrahedron with one corner truncated so that the interior can be seen. The light green/blue color represents the solvent-accessible surface. Three access apertures can be seen between each of the vertices shown.

cluster family and provides an estimate of volume in the tetrahedral-shaped M_4L_4 cavity. The effective edge length of the tetrahedral cavity is approximately the metal-to-metal distance minus 4 Å (to account for ligand and metal ion van der Waals radii). The calculations show that, for $[Ga_4\mathbf{L}^2_4]^{12-}$, the metal-to-metal distance is just under 19 Å and the cavity volume is approximately 450 Å^3, based on an optimized empty host structure. One would anticipate the cluster to accommodate slightly larger guest molecules without significant ligand distortion (Buckminsterfullerene, with a van der Waals volume of 520 Å^3, is pictured in Figure S1 in the Supporting Information). In the van der Waals surface view of the $[Ga_4\mathbf{L}^2_4]^{12-}$ molecular model, the interior of the tetrahedral-shaped cavity is shielded by aromatic groups but remains visible through six small gaps between the ligands (Figure 4).

Modeling of the biphenylene-bridged ligand $H_6\mathbf{L}^3$ (Scheme 1) indicates a metal-to-metal distance of 26.5 Å for the $[Ga_4\mathbf{L}^3_4]^{12-}$ cluster in comparison to 19.0 Å for the $[Ga_4\mathbf{L}^2_4]^{12-}$ tetrahedron. The calculations predict a very flexible wire-cage structure with poorly defined interior versus exterior (see Figure S2 in the Supporting Information). The biphenylene spacers between the central benzene core and the chelators increase the flexibility and conformational freedom

(35) Johnson, D. W.; Raymond, K. N. *Inorg. Chem.* **2001**, *40*, 5157−5161.
(36) Beissel, T.; Powers, R. E.; Parac, T. N.; Raymond, K. N. *J. Am. Chem. Soc.* **1999**, *121*, 4200−4206.
(37) CAChe 5.04 ed. Fujitsu Limited, 2002.

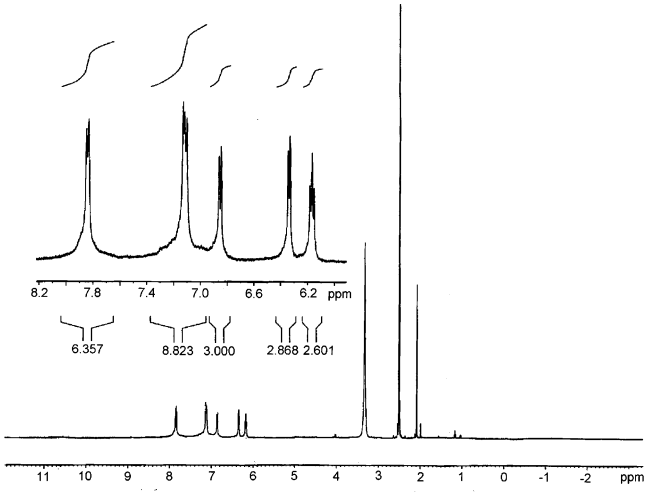

Figure 5. ^{1}H NMR spectrum of $K_{12}[Ga_4\mathbf{L}^2_4]$ in DMSO-d_6. The simplicity of the aromatic region indicates that the ligand protons within the metal−ligand cluster are in chemically equivalent positions. Effectively, each ligand chelate arm is related to another chelate arm by the rotational symmetry of the tetrahedron. Integration of the peaks in the aromatic region is normalized to 24 H atoms, which corresponds to the number of protons in each ligand $\mathbf{L}^2$.

in the ligand. As a result, the chelate vectors no longer lie in the same plane as that required in the M_4L_4 design scheme and self-assembly of a $M_4\mathbf{L}^3_4$ tetrahedron (M = Al(III), Ga(III) and Ti(IV)) was not observed. The failure of $H_6\mathbf{L}^3$ to form $M_4\mathbf{L}^3_4$ tetrahedra highlights the difficulty of controlling the conformation of large molecular components in a large supramolecular system.

$[M_4\mathbf{L}^2_4]^{12-}$ (M = Al(III), Ga(III), In(III)) Tetrahedra. The self-assembly of $[M_4\mathbf{L}^2_4]^{12-}$ clusters was performed under nitrogen in methanol. The tetrahedral assemblies are formed regardless of guest template availability. Equimolar amounts of the ligand $H_6\mathbf{L}^2$ and metal ions (as the acetyl acetonate salt) were combined in methanol. The ligand dissolved upon the addition of 12 equiv of a hydroxide base (KOH, NaOH, NMe_4OH). Generally, the reaction mixture was stirred for 2−16 h, with no observable difference in product yield. The ^{1}H NMR spectrum of $K_{12}[Ga_4\mathbf{L}^2_4]$ in DMSO-d_6 is shown in Figure 5 and is representative of the ^{1}H NMR spectra of the clusters with other trivalent metal ions (M = Al(III) and In(III)). All proton signals are shifted significantly from corresponding peaks in the deprotonated form of the free ligand. The simplicity of six sharp peaks (there are two overlapping signals between 7.1 and 7.2 ppm corresponding to integrated values of 3 and 6 protons, respectively) in the aromatic region of the ^{1}H NMR spectrum indicates that the 3-fold symmetry axis of each ligand coincides with a 3-fold symmetry axis of the overall tetrahedral assembly and each of the three chelate arms in one ligand and each of the four ligands within one metal−ligand ensemble are in chemically equivalent environments. Given the constraints of ligand geometry, the simultaneous requirements of satisfying metal and ligand coordination numbers and the presence of both 2- and 3-fold symmetry axes in the ligand and the overall ensemble, we assign the structure as the $M_4\mathbf{L}^2_4$ tetrahedral assembly. Simplicity in the ^{1}H NMR spectra of highly symmetric clusters, due to

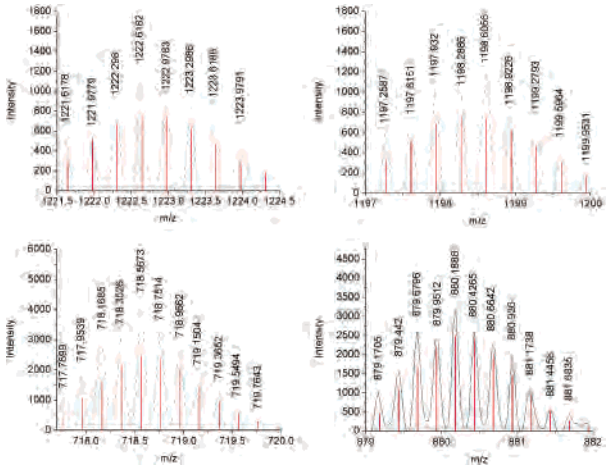

Figure 6. High-resolution electrospray mass spectra and isotopic simulation (red bars) of $K_xH_y(NMe_4)_z[Ga_4\mathbf{L}^2_4]$. Selected major peaks clockwise from top left: $\{H_4(NMe_4)_5[Ga_4\mathbf{L}^2_4]\}^{3-}$ (m/z = 1222.6182); $\{H_5(NMe_4)_4[Ga_4\mathbf{L}^2_4]\}^{3-}$ (m/z = 1198.6056); $\{H_5(NMe_4)_3[Ga_4\mathbf{L}^2_4]\}^{4-}$ (m/z = 880.1888); and $\{H_3(NMe_4)_4[Ga_4\mathbf{L}^2_4]\}^{5-}$ (m/z = 718.5673).

geometric equivalency of ligands related by symmetry, has been characteristic of both M_4L_4 and M_4L_6 tetrahedral clusters.[22,23,26,31,35,36]

The electrospray mass spectrometry data (ESI-MS) confirm the $[Ga_4\mathbf{L}^2_4]^{12-}$ stoichiometry (Figure S3 in the Supporting Information). In the potassium salt spectrum of $[Ga_4\mathbf{L}^2_4]^{12-}$, each cluster of peaks corresponds to a given charge state containing differing ratios of potassium, sodium (a ubiquitous contaminant), and protons. For example, the cluster of peaks between approximately m/z = 850−900 corresponds to the 4− charge state of the $[Ga_4\mathbf{L}^2_4]^{12-}$ cluster (partial list of peak assignment: m/z = 863 $\{K_4H_4[Ga_4\mathbf{L}^2_4]\}^{4-}$, 869 $\{K_4NaH_3[Ga_4\mathbf{L}^2_4]\}^{4-}$, 872 $\{K_5H_3[Ga_4\mathbf{L}^2_4]\}^{4-}$, 878 $\{K_5NaH_2[Ga_4\mathbf{L}^2_4]\}^{4-}$, 882 $\{K_6H_2[Ga_4\mathbf{L}^2_4]\}^{4-}$, 891 $\{K_7H[Ga_4\mathbf{L}^2_4]\}^{4-}$, and 897 $\{K_7Na[Ga_4\mathbf{L}^2_4]\}^{4-}$). Likewise, the same analysis performed on the group of peaks representing the 5− charge state centering on m/z = 683 $\{K_3H_4[Ga_4\mathbf{L}^2_4]\}^{5-}$ unambiguously shows the $[Ga_4\mathbf{L}^2_4]^{12-}$ stoichiometry. Additionally, simulation of major peaks in the high-resolution ESI-MS data of $K_x(NMe_4)_yH_z[Ga_4\mathbf{L}^2_4]$ strongly supports the assigned $[Ga_4\mathbf{L}^2_4]^{12-}$ composition (Figure 6).

Due to the mono-isotopic abundance of sodium and aluminum, the spectrum of the sodium salt of $[Al_4\mathbf{L}^2_4]^{12-}$ contains fewer but more intense peaks than the potassium/gallium analogue (Figure S4 in the Supporting Information). Groups of peaks corresponding to 4−, 5−, and 6− charge states are prominent. The largest peaks from each group of peaks within a given charge state are: m/z = 809 $\{Na_5H_3[Al_4\mathbf{L}^2_4]\}^{4-}$ 639 $\{Na_3H_4[Al_4\mathbf{L}^2_4]\}^{5-}$ and 529 $\{Na_2H_4[Al_4\mathbf{L}^2_4]\}^{6-}$. Furthermore, high-resolution ESI-MS data of $K_x(NMe_4)_yH_z[Al_4\mathbf{L}^2_4]$ matches the simulated spectra of major peaks in different charge states, thereby confirming the stoichiometry of the $[Al_4\mathbf{L}^2_4]^{12-}$ clusters (Figure 7).

$[Ti_4\mathbf{L}^2_4]^{8-}$ Tetrahedron. On the basis of the approach angle analysis described earlier, Ti(IV) ions are ideally suited to the formation of M_4L_4 clusters because of the lower twist angle in comparison to Al(III), Ga(III), and Fe(III) triscatecholates. Surprisingly, formation of the titanium cluster

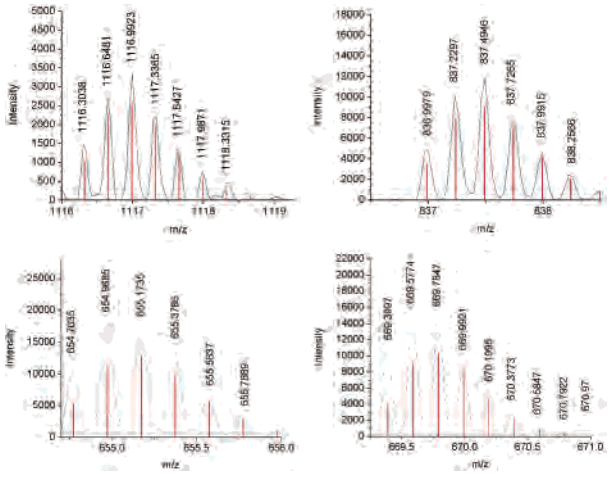

Figure 7. High-resolution electrospray mass spectra and isotopic simulation (red bars) of $K_xH_y(NMe_4)_z[Al_4\mathbf{L}^2_4]$. Selected major peaks clockwise from top left: $\{H_6(NMe_4)_3[Al_4\mathbf{L}^2_4]\}^{3-}$ (m/z = 1116.9923); $\{H_5(NMe_4)_3[Al_4\mathbf{L}^2_4]\}^{4-}$ (m/z = 837.4946); $\{H_5(NMe_4)_2[Al_4\mathbf{L}^2_4]\}^{5-}$ (m/z = 669.7847); and $\{H_4(NMe_4)_3[Al_4\mathbf{L}^2_4]\}^{5-}$ (m/z = 655.1735).

was not observed under conditions previously utilized for the synthesis of the $[Ti_4\mathbf{L}^1_4]^{8-}$ clusters (in dimethylformamide at 150 °C).[26] Instead, formation of the $[Ti_4\mathbf{L}^2_4]^{8-}$ tetrahedron occurs in methanol at reflux. Given the kinetic inertness of the tetravalent titanium ions, this observation was somewhat unexpected and we suggest a solvent-assisted formation mechanism that proceeds via a titanium-methoxy intermediate. Once formed, the $[Ti_4\mathbf{L}^2_4]^{8-}$ cluster is stable under various solvent and pH conditions.

The ^{1}H NMR spectrum (Figure 8) of $K_8[Ti_4\mathbf{L}^2_4]$ in MeOD-d_4 differs from the spectra of the trivalent metal ion analogues $[M_4\mathbf{L}^2_4]^{12-}$ (M = Al(III), Ga(III), In(III)). Rather than six aromatic proton signals in addition to an amide proton signal, the spectrum of $K_8[Ti_4\mathbf{L}^2_4]$ shows three large aromatic signals and one sharp amide proton signal. A closer scrutiny of the peak shape and integration data reveals overlap within two of the three large aromatic peaks. There are in fact a total of six aromatic signals. Again, the simplicity in the aromatic region indicates that the ligands within the coordination framework are symmetrically related and are therefore in chemically equivalent positions. The overlap of aromatic signals in $K_8[Ti_4\mathbf{L}^2_4]$ is apparently coincidental since separation of the overlapping peaks into six distinct peaks occurs when the potassium counterions are replaced with NMe_4^+ or NEt_4^+ ions, which can be encapsulated within the cavity and thus alter the conformation of the phenylene groups on the ligand core.

In the ESI-MS spectrum of $K_8[Ti_4\mathbf{L}^2_4]$ (Figure 9, high-resolution ESI-MS spectrum of $K_xH_y[Ti_4\mathbf{L}^2_4]$ is shown in Figure S5), three different charge states of the cluster are visible: 3− (approximate range m/z = 1095−1125), 4− (approximate range m/z = 802−841), and 5− (approximate range m/z = 642−667). Analysis of the largest peak within each charge state is as follows m/z = 1108.6 $\{K_3H_2[Ti_4\mathbf{L}^2_4]\}^{3-}$, 802.8 $\{H_4[Ti_4\mathbf{L}^2_4]\}$,$^{4-}$ and 641.9 $\{H_3[Ti_4\mathbf{L}^2_4]\}^{5-}$. Additionally, high-resolution ESI-MS data of $K_x(NMe_4)_yH_z[Ti_4\mathbf{L}^2_4]$ have also been simulated by isotopic modeling to confirm the $[Ti_4\mathbf{L}^2_4]^{8-}$ stoichiometry (Figure 10).

While we judged the titanium analogue of $M_4\mathbf{L}^2_4$ as the most promising candidate for crystallization, X-ray diffraction of single crystals of $[Ti_4\mathbf{L}^2_4]^{8-}$ with various counterions showed poor long-range ordering and maximum high-angle data corresponding to a resolution of only 1.5 Å.

Guest Selectivity in $[Ga_4\mathbf{L}^2_4]^{12-}$ and $[Ti_4\mathbf{L}^2_4]^{8-}$. The anionic $M_4\mathbf{L}^2_4$ (M = Ga(III), Ti(IV)) tetrahedra encapsulate monocations of appropriate size and shape. They do not encapsulate anions, neutral molecules, or multiply charged cations. Guest molecule affinity studies by ^{1}H NMR spectroscopy show that both tetraethylammonium (NEt_4^+, 360 Å^3) and tetraethylphosphonium (PEt_4^+, 390 Å^3) ions are encapsulated in the cavities of the $M_4\mathbf{L}^2_4$ clusters, as evidenced by 1.5−2 ppm upfield shifts of proton signals assigned to the encapsulated guest species. The ^{1}H NMR spectrum of NEt_4^+ encapsulated in the $[Ti_4\mathbf{L}^2_4]^{8-}$ tetrahedron is shown in Figure 11. Integration of the peaks originating from the encapsulated NEt_4^+ ion indicates exactly one encapsulated guest molecule per tetrahedral host. Additional ammonium and phosphonium cations remain outside the host and resonate at the same chemical shift as samples of the free ammonium ion in the absence of the $M_4\mathbf{L}^2_4$ clusters. Tetrapropylammonium ions (770 Å^3) are not encapsulated, apparently because they are significantly larger than the estimated cavity volume (450 Å^3).

While the tetrapropylammonium result demonstrates an upper limit for guest size in the cavity of the $M_4\mathbf{L}^2_4$ tetrahedron, there is also size discrimination for guest molecules that are far smaller than the cavity. When tetramethylammonium (NMe_4^+, <150 Å^3) is added to a solution of the $M_4\mathbf{L}^2_4$ cluster, there is no evidence of an upfield-shifted peak indicative of an encapsulated species in the ^{1}H NMR spectrum. However, there are some shifts of the aromatic signals as a result of added tetramethylammonium. This shift is particularly notable in the case of $[Ti_4\mathbf{L}^2_4]$,$^{8-}$ in which the overlapping sets of aromatic signals become completely resolved upon addition of tetramethylammonium. This observation can be explained by very weak binding of the small tetramethylammonium cation in the cavity. The absence of a signal corresponding to encapsulated tetramethylammonium suggests that this small guest molecule is in rapid exchange with external cations; even upon cooling the sample to −40 °C, no NMR signal for encapsulation is observed. Nevertheless, there is sufficient interaction between tetramethylammomium and the proximal protons on the 1,3,5-triphenylbenzene ligand backbone in $[Ti_4\mathbf{L}^2_4]^{8-}$ to induce a shift of aromatic proton signals.

In addition to guest size selectivity, the tetrahedral-shaped cavity of the $M_4\mathbf{L}^2_4$ cluster is also selective for guest shape. Cylindrical- rather than tetrahedral-shaped molecules with smaller or comparable volume to tetraethylammonium, such as bis(cyclopentadienyl)cobaltocenium (190 Å^3) and bis-(decamethylcyclopentadienyl)cobaltocenium (450 Å^3) ions, are not encapsulated.

Chiral Induction in $[Ga_4\mathbf{L}^1_4]^{12-}$ and $[Ga_4\mathbf{L}^2_4]^{12-}$. One of the unique features of the tris-catecholate metal−ligand coordination assemblies is the inherent chirality originating from the tris-bidentate metal chelates. In theory, the metal

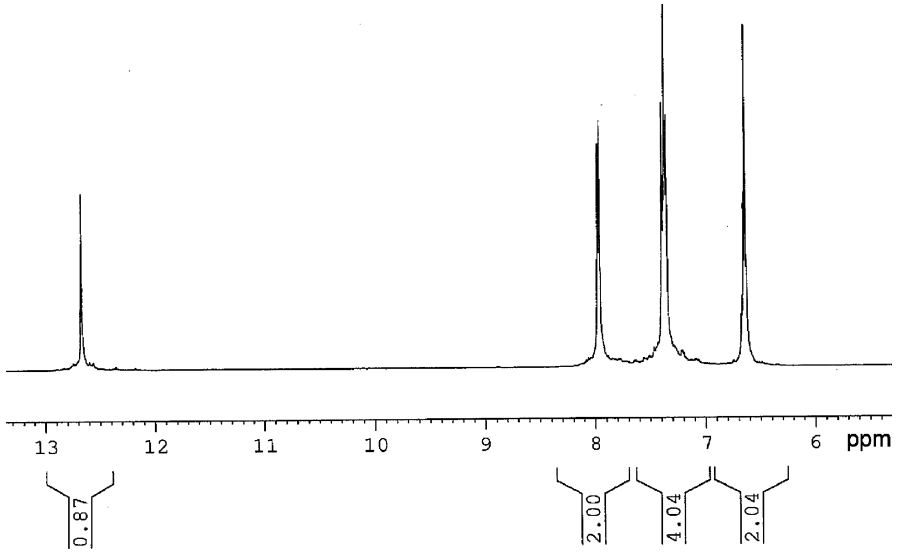

Figure 8. ^{1}H NMR spectrum of $K_8[Ti_4\mathbf{L}^2_4]$ in MeOD-d_4. The simplicity in the aromatic region indicates that the ligands within the metal−ligand cluster are in chemically equivalent positions and each ligand chelate arm is related to another chelate arm by symmetry. Integration of the aromatic peaks is normalized to 8 H, which corresponds to one-third the number of protons in each of the 3-fold symmetric ligand $\mathbf{L}^2$. The peak at 12.7 ppm corresponds to the amide proton.

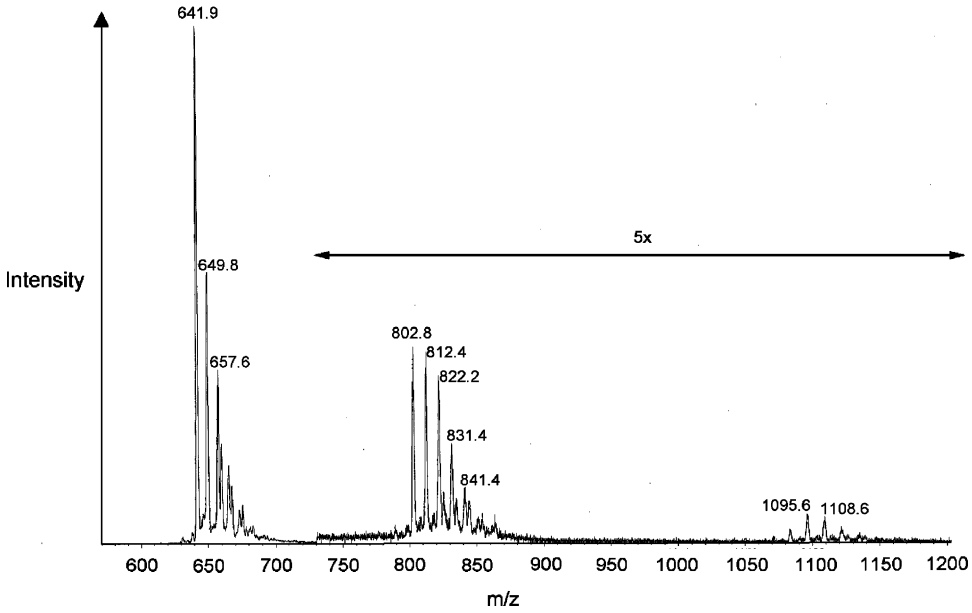

Figure 9. ESI-MS spectrum of $K_8[Ti_4\mathbf{L}^2_4]$ in MeOH. Three different charge states of the cluster are visible: 3− (approximate range m/z 1095−1125), 4− (approximate range m/z 802−841), and 5− (approximate range 642−667). Analysis of the largest peak within each charge state: $m/z = 1108.6$ $\{K_3H_2[Ti_4\mathbf{L}^2_4]\}^{3-}$, $m/z = 802.8$ $\{H_4[Ti_4\mathbf{L}^2_4]\}^{4-}$ and $m/z = 641.9$ $\{H_3[Ti_4\mathbf{L}^2_4]\}^{5-}$. The other peaks within each charge state originate from proton/potassium exchanges.

centers within each tetranuclear structure can adopt either Δ or Λ chirality or a combination thereof. As a consequence, the M_4L_4 structure can adopt T (ΔΔΔΔ or ΛΛΛΛ), C_3 (ΛΔΔΔ or ΔΛΛΛ), or S_4 (ΔΔΛΛ) symmetry. Experimentally, the NMR data for both $M_4\mathbf{L}^1_4$ and $M_4\mathbf{L}^2_4$ clusters are consistent with T-symmetric structures and not C_3 or S_4 symmetries. Furthermore, the crystal structure of the previously reported $[Ti_4\mathbf{L}^1_4]^{8-}$ tetrahedron shows identical chirality at all four metal centers.[26]

Previously, the chiral cation, (*S*)-1-methyl-2-(1-methylpyrrolidin-2-yl)-pyridinium iodide (**s-nic**), has been shown to induce an enantiomeric excess in a racemic population of M_2L_3 helicates and M_4L_6 tetrahedra.[38,39] While it is understood that the mechanism of chiral induction is primarily dependent on asymmetric interaction of **s-nic** with the tris-catecholate metal caps in the supramolecular coordination assembly, circular dichroism, NMR, and crystallographic data suggested that conformation of the aryl backbone attached to the amide moiety of the catecholate also strongly influences the effectiveness of chiral induction.[40] Chiral induction in M_4L_4 tetrahedra has not been investigated previously. Although some degree of chiral induction with chiral cations is anticipated because the M_4L_4 tetrahedra contain tris-

(38) Terpin, A. J.; Ziegler, M.; Johnson, D. W.; Raymond, K. N. *Angew. Chem., Int. Ed.* **2001**, *40*, 157−160.
(39) Yeh, R. M.; Ziegler, M.; Johnson, D. W.; Terpin, A. J.; Raymond, K. N. *Inorg. Chem.* **2001**, *40*, 2216−2217.
(40) Yeh, R. M., Raymond, K. N., manuscript in preparation.

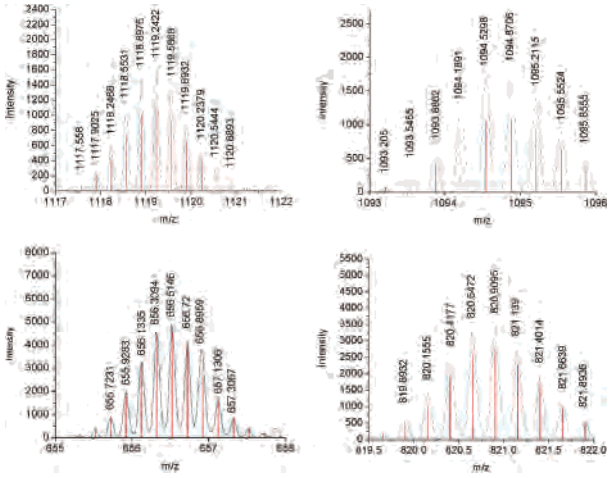

Figure 10. High-resolution electrospray mass spectra and isotopic simulation (red bars) of $K_xH_y(NMe_4)_z[Ti_4\mathbf{L}^2_4]$. Selected major peaks clockwise from top left: $\{H_3(NMe_4)_2[Ti_4\mathbf{L}^2_4]\}^{3-}$ (m/z = 1119.2422); $\{H_4(NMe_4)_1[Ti_4\mathbf{L}^2_4]\}^{3-}$ (m/z = 1094.8706); $\{H_3(NMe_4)_1[Ti_4\mathbf{L}^2_4]\}^{4-}$ (m/z = 820.9095); and $\{H_2(NMe_4)_1[Ti_4\mathbf{L}^2_4]\}^{5-}$ (m/z = 656.5146).

catecholate-coordinated metal centers, the level of chiral induction and the persistence of enantiomeric enrichment in the M_4L_4 tetrahedra are expected to differ from the M_4L_6 tetrahedra and M_2L_3 helicates.

When the small $[Ga_4\mathbf{L}^1_4]^{12-}$ tetrahedron is synthesized in the presence of **s-nic**, enantiomeric enrichment is observed (Figure S6 in the Supporting Information). In contrast, the larger phenylene-expanded $[Ga_4\mathbf{L}^2_4]^{12-}$ tetrahedron shows a negligible level of enantiomeric enrichment when synthesized in the presence of **s-nic**. One possible reason for the lack of chiral induction is the additional rotational freedom of the phenylene spacers in $H_6\mathbf{L}^2$. Molecular modeling studies have shown that these phenylene spacers between the amide linkages and the 1,3,5-substituted central ring are rotated out of the central scaffold plane. There is no steric constraint that mechanically couples the rotational direction of the phenylene spacer groups on the three ligand arms. In solution, the backbone conformation of the ligand is in dynamic equilibrium and coupling of conformation from one ligand arm to another is weak.

The apparent *T* symmetry of the cluster as seen in the NMR spectra is consistent with three possible explanations: 1) The cluster is homochiral and has *T* symmetry on the NMR time scale. 2) The cluster has vertexes of mixed chirality, but these interchange rapidly on the NMR time scale, resulting in a time-average *T* symmetry. 3) The flexibility of the poly(phenylene)-bridged ligand backbone and the remoteness from the differing chiral metal centers make the protons magnetically equivalent. We do not have sufficient information to distinguish between these scenarios, but the slow rate of isomerism in simple tris-(bidentate) catecholate complexes of Al(III) and the apparent *T* symmetry seen in the $[Al_4\mathbf{L}^2_4]^{12-}$ complexes leads us to reject explanation 2.[32]

Comparison between M_4L_4 and M_4L_6 Tetrahedra Designs. In their roles as supramolecular hosts, there are significant differences between the M_4L_4 and M_4L_6 tetrahedra in terms of self-assembly, guest selectivity, host stability, and chirality. From the perspective of self-assembly, the face-on approach (M_4L_4) has several fundamental advantages over the edge-on approach (M_4L_6). First, the stability of the M_4L_4 tetrahedron is expected to be higher than that of the M_4L_6 tetrahedron because of higher denticity of the ligand in the M_4L_4 structure. Indeed, during the course of ESI-MS data acquisition, we observed intact $M_4\mathbf{L}^2_4$ (M = Al(III), Ga(III)) tetrahedra at more than twice the ionization voltage that caused complete fragmentation of the $M_4\mathbf{L}^N_6$ (M = Al(III), Ga(III)) tetrahedra. This observation is indicative of higher stability of the $M_4\mathbf{L}^2_4$ assemblies in the gas phase compared to $M_4\mathbf{L}^N_6$ assemblies. The entropic cost of self-assembly is lower for the M_4L_4 structure with four ligands than for the M_4L_6 structure with six ligands. This smaller free energy penalty is the reason for higher stability. Second, the smallest possible discrete, closed structure for a combination of rigid 3-fold symmetric tris-bidentate ligands and pseudo-octahedral, six-coordinate metal ions is M_4L_4, whereas for the 2-fold symmetric bis-bidentate ligands, formation of a lower stoichiometry M_2L_3 helicate is a possible alternative to the M_4L_6 tetrahedron. For these two reasons, one would choose the M_4L_4 approach if the goal is strictly to build a coordination tetrahedron without regard for properties such as cavity shape, size, accessibility, and chirality.

Three important structural differences between the M_4L_4 and the M_4L_6 tetrahedra as supramolecular hosts are the size, shape, and accessibility of the cavity. For a given maximum coordination cage diameter defined by metal-to-metal distance, the M_4L_4 tetrahedron design has an inherently smaller cavity size as compared to that of the M_4L_6 cluster. For example, the estimated maximum cavity volume in the $M_4\mathbf{L}^2_4$ cluster with a metal-to-metal distance of 19 Å is approximately 450 Å^3, whereas the cavity volume in a hypothetical M_4L_6 cluster with the same metal-to-metal distance is 2400 Å^3. As a consequence, the M_4L_4 design is not the most efficient route toward generating the largest possible cavity.

The shape of the M_4L_4 cavity is nearly tetrahedral, rather than nearly cubic as in the M_4L_6 cluster, and this difference has a profound effect on the shape of guest molecules that can be encapsulated. Shape selectivity has been shown by ^{1}H NMR spectroscopy, indicating inclusion of tetrahedrally shaped tetraethylammonium and tetraethylphosphonium cations into $M_4\mathbf{L}^2_4$ tetrahedra but not cylindrically shaped bis-(cyclopentadienyl)-cobaltocenium ions (vdW volume = 190 Å^3) despite a much smaller van der Waals volume.[41] In contrast, the $M_4\mathbf{L}^N_6$ naphthalene-based tetrahedron has a similar volume as $M_4\mathbf{L}^2_4$ but a cubic-shaped cavity. This cubelike cavity encapsulates bis(cyclopentadienyl)-cobaltocenium and the larger bis(decamethylcyclopentadienyl)-cobaltocenium ions (vdW volume = 450 Å^3), as well as other bulky, irregularly shaped organometallic half-sandwich complexes.[14−17,41]

Last, the $M_4\mathbf{L}^2_4$ tetrahedra have more accessible cavities than $M_4\mathbf{L}^N_6$ tetrahedra of similar volume. This difference influences guest exchange rates because guest exchange is

(41) Bondi, A. *J. Phys. Chem.* **1964**, *68*, 441−451.

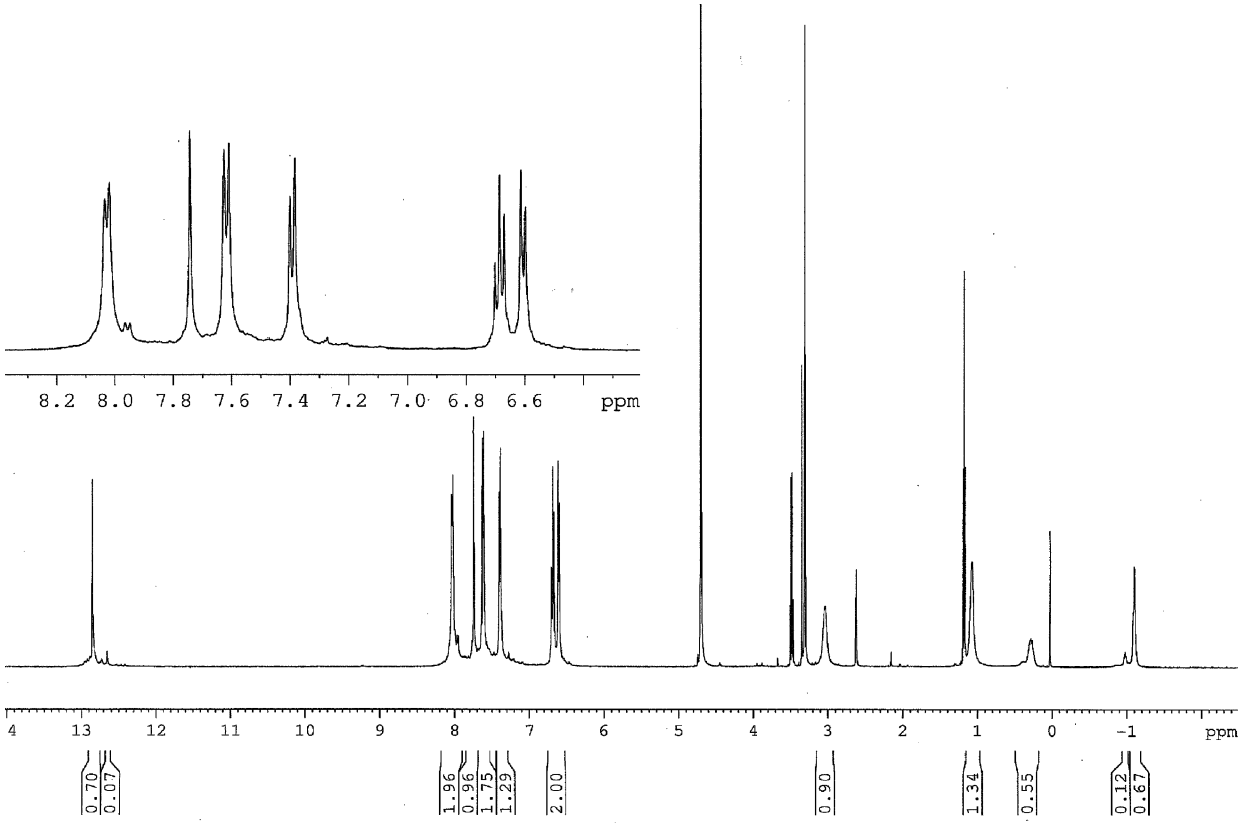

Figure 11. ^{1}H NMR spectrum of $K_8[Ti_4\mathbf{L}^2{}_4] \subset NEt_4^+$] in MeOD-$d_4$. The ^{1}H NMR signals for the encapsulated NEt_4^+ ion appear at 0.28 (methylene protons) and −1.10 ppm (methyl protons). External NEt_4^+ ions are either ion-paired to the outside of the anionic cluster or solvated. The signals for the external NEt_4^+ ions appear at 3.04 (methylene protons) and 1.07 ppm (methyl protons). The aromatic region is different for the host−guest complex than for the host alone (compare to Figure 8). This effect has been observed previously for M_4L_6-type tetrahedra.

believed to occur through a nondissociative mechanism via enlargement of natural cluster openings through a concerted distortion of the supermolecule.[32] The absence of an encapsulated NMe_4^+ signal in the ^{1}H NMR spectrum of $M_4\mathbf{L}^2{}_4$ clusters is in contrast to the observation of a broadened signal of encapsulated NMe_4^+ in the $M_4\mathbf{L}^N{}_6$ assemblies. These data indicate a faster guest exchange rate for the $M_4\mathbf{L}^2{}_4$ architecture and support the modeling studies that show a more accessible cavity in the $M_4\mathbf{L}^2{}_4$ than in $M_4\mathbf{L}^N{}_6$ tetrahedra.

Summary

The design and synthesis of large $M_4\mathbf{L}^2{}_4$ tetrahedra extends our initial design approach of M_4L_4 tetrahedra formation in which four pseudo-octahedral metal centers are coordinated by four 3-fold symmetric ligands. The phenylene linker extension in ligand $H_6\mathbf{L}^2$ enables the formation of tetrahedra with a cavity size of approximately 450 Å^3. As a result, charge-, size-, and shape-selective guest encapsulation is observed. In contrast, the biphenylene extended ligand $H_6\mathbf{L}^3$ is conformationally too flexible to form M_4L_4 assemblies. The inability of $H_6\mathbf{L}^3$ to form the desired $M_4\mathbf{L}^3{}_4$ tetrahedral architecture points to the importance of geometric and conformational rigor in this design approach. Finally, variations in host−guest encapsulation properties between $M_4\mathbf{L}^2{}_4$ and $M_4\mathbf{L}^N{}_6$ clusters are explained by their differences in cavity shape and accessibility. Studies are underway to further investigate the differences in guest exchange dynamics between these two types of tetrahedral cluster architectures, as well as to overcome the increased flexibility of the large ligands in order to assemble still larger M_4L_4 tetrahedra.

Experimental Procedures

General Methods. Unless otherwise specified, all starting materials were purchased from commercial sources and used without further purification. Anhydrous potassium phosphate and anhydrous potassium acetate were dried under vacuum at 120 °C and stored in the drybox. All palladium catalysts with the exception of $PdCl_2(dppf)\cdot CH_2Cl_2$ were stored in the drybox. Manipulations were performed under normal atmospheric conditions unless otherwise noted. All NMR spectra were recorded using Bruker AV300, AVB400, AVQ400, and DRX500 spectrometers rated at 300, 400, 400, and 500 MHz, respectively, for ^{1}H. The NMR peaks are reported as shifts (ppm) downfield from TMS and referenced to residual solvent protons. Electrospray mass spectra were obtained on a Finnigan LCQ quadrupole ion trap mass spectrometer equipped with a microspray ionization source (Finnigan MAT, San Jose, CA). High-accuracy and -resolution electrospray mass spectra were obtained on an Agilent LC/MSD TOF spectrometer at The Scripps Research Institute Mass Spectrometry Facility. FAB mass spectra and elemental analysis were performed by the University of California Berkeley College of Chemistry Analytical Facility. Circular Dichroism spectra were obtained on a Jasco J-810 spectropolarimeter.

1,3,5-Tris(4′-nitrophenyl)benzene. Potassium pyrosulfate (99 g. 0.39 mol) was heated in a crucible with a Bunsen burner until the solid completely melted and the molten material was fuming. The dish was then cooled to room temperature (RT), and the solidified potassium pyrosulfate was crushed and stored in a

desiccator. 4-Nitroacetophenone (49.5 g, 0.39 mol) in a 250 mL round-bottom flask (equipped with a 2 in. magnetic stirrer) was melted by heating in an oil bath. Concentrated sulfuric acid (4 mL) was added while stirring. The dry, crushed potassium pyrosulfate was added with stirring, and the temperature of the mixture was raised to 95 °C. The solution became viscous and then solidified in 2−3 h. The heating was continued overnight, and an almost black solid was obtained. The solid pellet was treated with boiling water to remove inorganic salts. The residue was then treated with hot chloroform three times to remove organic impurities. The greenish deep brown solid was vacuum-dried (yield: 20.5 g, 45%). Anal. Calcd for $C_{24}H_{15}N_3O_6$: C, 65.31 (64.93); H, 3.43 (3.11); N, 9.52 (9.17). Since this compound was not soluble in common solvents, it was not characterized spectroscopically, but was directly used in further syntheses.

1,3,5-Tris(4′-aminophenyl)benzene. To a slurry of 1,3,5-tris-(4′-nitrophenyl)benzene (8.8 g, 20 mmol) and tin granules (47 g, 0.40 mol) in ethanol (20 mL), concentrated HCl (12 N, 200 mL) was added slowly with vigorous stirring under reflux. After 8 h, the reaction mixture was cooled to RT and the precipitate was collected by filtration. The solid was dissolved in water (200 mL) and filtered to remove residual tin. The filtrate was treated with NaOH solution (30%). The product was precipitated by triturating the solution, collected by filtration, washed with water repeatedly, and dried under vacuum. Pale yellow product was obtained. (6.2 g, 90%) ^{1}H NMR (500 MHz, D_2O−DCl) δ: 6.024 (s, 3H, benzeneArH), 6.388 (d, J = 8.0 Hz, 6H phenylArH), 6.249 (d, J = 9.5 Hz, 6H phenylArH). ^{13}C NMR (125 MHz, D_2O−DCl) δ: 122.5, 122.9, 127.2, 128.1, 137.7, 139.1.

4-Bromo-(2′,3′-dimethoxybenzamido)benzene. A Schlenk flask was charged with 4-bromoaniline (9.45 g, 55 mmol), 2,3-dimethoxybenzoic acid chloride (11.0 g, 55 mmol), NEt_3 (8.5 mL, 60.5 mmol), and degassed CH_2Cl_2 (400 mL, dried over alumina sieves). The solution was filtered after 12 h of stirring at room temperature. The filtrate was washed with 1 M NaOH (3 × 100 mL) and 1 M HCl (3 × 100 mL). Upon being dryed with sodium sulfate, the CH_2Cl_2 solution was evaporated to yield a solid product. The solid was dissolved in a small volume of ethanol at reflux and allowed to cool slowly to room temperature. Large, off-white crystalline product was isolated. A second crop of product was isolated from a reduced volume of the ethanol (15.4 g, 84%). FAB MS m/z (%) 336 (40) $[M]^+$. ^{1}H NMR (400 MHz, $CDCl_3$) δ: 10.08 (s, 1H), 7.78 (dd, J = 8 Hz, J 1.6 Hz, 1H), 7.60 (d, J = 9.2 Hz, 2H), 7.48 (d, J = 9.2 Hz, 2H), 7.22 (t, J = 8 Hz, 1H), 7.12 (dd, J = 8 Hz, J 1.6 Hz, 1H), 3.94 (s, 3H), 4.00 (s, 3H). ^{13}C NMR (100 MHz, DMSO-d_6) δ: 165.4, 152.9, 146.2, 138.8, 131.9, 131.6, 124.6, 121.9, 120.3, 115.5, 115.1, 110.4, 61.5, 59.3, 30.8. Anal. Calcd (Found) for $C_{15}H_{14}BrNO_3$: C, 53.59 (53.87); H, 4.20 (4.53); N, 4.17 (4.05).

4-Pinacolatoboronic Ester-(2′,3′-dimethoxybenzamido)benzene. A dry Schlenk flask was charged with 4-bromo-(2′,3′-dimethoxybenzamido)benzene (1.8 g, 5.2 mmol), bis-pinacolatodiborane (1.5 g, 5.7 mmol, 1.1 equiv), $Pd_2(DBA)_3$ (3 mol% with respect to Pd, 80 mg, DBA = dibenzylideneacetone), tricyclohexylphosphine (98 mg, 2 equiv per Pd), and anhydrous KOAc (0.85 g) under a dinitrogen atmosphere. Dry, degassed DMSO (20 mL) was added to the solid. The mixture was stirred for 2 h at 90 °C and 12 h at 70 °C. Water and brine (1:1, 250 mL total) were added to the solution after it had cooled to room temperature. The aqueous/DMSO mixture was extracted with benzene (100 mL × 3). The combined organic layer was washed with water (100 mL) and brine (100 mL) and dried over sodium sulfate. Flash silica column chromatography, eluting with 40:1 $CHCl_3$/EtAc, yielded 2.1 g of white solid (1.8 g, 88% yield). ^{1}H NMR (400 MHz, $CDCl_3$) δ: 10.05 (s), 7.83 (d, J = 9.5 Hz, 2H), 7.78 (dd, J = 8.0, 1.6 Hz, 1H), 7.70 (d, J = 9.5 Hz, 2H), 7.20 (t, J = 8.0 Hz, 1H), 7.08 (dd, J = 8.0, 1.6 Hz, 1H), 3.99 (s, 3H), 3.91 (s, 3H), 1.34 (s, 12H). Anal. Calcd (Found) for $C_{21}H_{26}BNO_3 \cdot 0.5(CHCl_3)$: C, 58.30 (58.42); H, 6.03 (6.39); N, 3.16 (3.17).

1,3,5-Tris(4′-(2″,3″-dibenzyloxybenzamido)phenyl)benzene (Bn_6L^2). To a solution of 1,3,5-tris(4′-aminophenyl)benzene (1.0 g, 3.0 mmol) and dry Et_3N (1 mL) in dry DMAA (25 mL), 2,3-dibenzyloxybenzoic acid chloride (3.5 g, 1.7 mmol) was added while stirring. The reaction mixture was stirred at 65 °C in a sealed flask for 15 h; the solvent was removed under vacuum. The residue was washed thoroughly with HCl (1 N), NaOH (1 N), and distilled water and dried in an vacuum oven to give 3.4 g (2.6 mmol, 87%) of pure product as a pale greenish yellow solid. ^{1}H NMR (500 MHz, DMSO-d_6) δ: 5.10 (s, 6H, $BzCH_2$), 5.25 (s, 6H, $BzCH_2$), 7.206 (d, 6H, J = 4.5 Hz, ArH), 7.250 (d, 6H, J = 4.5 Hz, ArH), 7.343 (d, 6H, J = 5.0 Hz, ArH), 7.355 (t, 3H, J = 7.0 Hz, ArH), 7.416 (t, 6H, J = 7.5 Hz, ArH), 7.524 (d, 6H, J = 7.5 Hz, ArH), 7.769 (d, 6H, J = 9 Hz, ArH), 7.847 (d, 6H, J = 8.0 Hz, ArH), 7.396 (s, 3H, AmideH). ^{13}C NMR (125 MHz, DMSO-d_6) δ: 70.65, 75.69, 120.33, 124.82, 127.77, 128.19, 128.43, 128.47, 128.65, 128.70, 128.92, 132.11, 137.42, 145.46, 152.10, 165.06. FAB-MS: m/z 1300.5 $[MH^+]$.

1,3,5-Tris(4′-(2″,3″-dimethoxybenzamido)phenyl)benzene (Me_6L^2). 4-Pinacolatoboronic ester-(2′,3′-dimethoxybenzamido)benzene (0.98 g, 2.56 mmol), 1,3,5-tribromobenzene (0.24 g, 0.77 mmol), tetrakis-(triphenylphosphine)palladium (0.011 g, 9.9 μmol), degassed toluene (60 mL), degassed ethanol (10 mL), and sodium carbonate solution (2 M, 2.5 mL) were combined in a 100 mL Schlenk flask under nitrogen. The mixture was heated to reflux for 17 h. The solvent was completely evaporated under vacuum. The residue was dissolved in chloroform (100 mL) and washed with water (3 × 40 mL). The organic layer was dried over magnesium sulfate and evaporated to dryness to yield 0.59 g of pale yellow solid (0.70 mmol, 90% yield). ^{1}H NMR (500 MHz, $CDCl_3$) δ: 3.813 (s, 9H, OCH_3), 3.923 (s, 9H, OCH_3), 6.989 (dd, 3H, J = 8.1, 1.4 Hz, ArH), 7.104 (t, 3H, J = 8.1 Hz, ArH), 7.634 (d, 6H, J = 8.6 Hz, ArH), 7.679 (s, 3H, ArH), 7.708 (dd, 3H, J = 8.1, 1.4 Hz, ArH), 7.736 (d, 6H, J = 8.6 Hz, ArH), 10.038 (s, 3H, AmideH). FAB-MS: m/z 844.3 $[MH^+]$.

1,3,5-Tris(4′-(2″,3″-dihydroxybenzamido)phenyl)benzene (H_6L^2). (a) 1,3,5-tris(4′-(2″,3″-dibenzyloxybenzamido)phenyl)benzene (1.3 g, 1.0 mmol) was suspended in CH_2Cl_2 (30 mL) in a Schlenk flask equipped with a Teflon stopcock. Under a flow of nitrogen, the slurry was cooled to −10 °C before BBr_3 (2.0 mL) was injected. The yellow slurry was stirred for 5 days before removal of the solvent and excess BBr_3 under vacuum. The remaining greenish-brown solid was heated to reflux in methanol (200 mL) for 12 h. The suspension was filtered while hot. The filtrate was concentrated to a small volume (20 mL), and the product was precipitated as a gray solid upon cooling. The precipitate was collected by filtration and dried under vacuum to give the pure product 0.58 g (76%).

(b) 1,3,5-Tris(4′-(2″,3″-dimethoxybenzamido)phenyl)benzene (0.59 g, 0.70 mmol) was dissolved in dry chloroform (100 mL), and an excess of BBr_3 (1.32 mL, 14 mmol) was added. After 5 days, water was added to quench the excess BBr_3. The gray solid was isolated by filtration and heated to reflux in methanol overnight. The suspension was filtered while hot. The filtrate was concentrated to a small volume (10 mL), and the product was precipitated as a gray solid upon cooling. Yield: 0.43 g (0.56 mmol, 80%). ^{1}H NMR (500 MHz, DMSO-d_6) δ: 6.796 (t, 6H, J = 7.8 Hz, ArH), 6.998 (d, 6H, J = 8.5 Hz, ArH), 7.483 (d, 6H, J = 7.5 Hz, ArH), 7.861

(d, 6H, J = 8.3 Hz, ArH), 7.913 (s, 3H, ArH), 7.921 (d, 6H, J = 8.4 Hz, ArH), 9.414 (s,br, 3H, AmideH), 10.453 (s, 3H, phenolH), 11.662 (s,br, 3H, phenolH). FAB MS: m/z 760.3 [MH^+]. Anal. Calcd (Found) for $C_{45}H_{33}N_3O_9$: C, 71.14 (70.93); H, 4.38 (4.11); N, 5.53 (5.11).

1,3,5-Tris(4′-(2‴,3‴-dibenzyloxybenzamido)-1′,1″-biphenyl)-benzene (Bn_6L^3). A Schlenk flask was charged with 1,3,5-tri(*p*-bromophenyl)benzene (0.12 g, 0.22 mmol), 4-(2′,3′-dibenzyloxybenzamido)benzyl pinacol boronic ester (0.50 g, 0.93 mmol), and anhydrous DMF (20 mL). Under a nitrogen atmosphere, $Pd(PPh_3)_4$ (55 mg, 5 mol %) and anhydrous K_3PO_4 tribasic (2 g, 9 mmol) were added. The mixture was stirred at 80 °C for 24 h under N_2. The mixture was evaporated to near dryness under vacuum at 80 °C. Chloroform (100 mL) and a 50% brine solution were added to the dark solid, and the layers were separated. Aqueous wash with 50% brine (50 mL) was repeated, followed by three washes with HCl (1 N) and one saturated brine wash. The chloroform layer was isolated, dried over sodium sulfate, and evaporated to about 2 mL. Silica column chromatography, eluting with $CHCl_3$/EtOAc (40:1) yielded the product. (Yield: 100 mg, 30%). ^{1}H NMR of product (400 MHz, DMSO-d_6) δ: 10.49 (s), 10.32 (m), 10.11 (m), 8.99 (s), 7.90−7.18 (m), 7.03 (t), 6.78 (m), 5.17 (sharp m). FAB-MS: m/z 1072 [M^+].

1,3,5-Tris(4′-(2‴,3‴-dihydroxybenzamido)-1′,1″-biphenyl)-benzene (H_6L^3). Bn_6L^3 (80 mg, 0.05 mmol) and BBr_3 (20 equiv) were combined in $CHCl_3$ (5 mL). After the reaction was stirred for 5 days, excess BBr_3 and solvent were evaporated under vacuum. Water (30 mL) was added, and the suspension was stirred for 20 h, heated to reflux for 1 h, and evaporated to dryness under vacuum at 70 °C. The solid was dissolved in acetone and filtered to remove some dark blue insoluble precipitate. The acetone solution was reduced in volume, and water was added to precipitate the product as a very fine white powder. The acetone/water product suspension was evaporated to dryness under vacuum. Yield (30 mg, 60%) ^{1}H NMR of product (400 MHz, DMSO) δ: 11.64 (bs, 3H) 10.46 (s), 10.25 (s), 9.46 (s, 3H), 7.98 (d, 3H), 7.87−7.74 (m, 12H), 7.55 (d, 3H), 7.40 (m, 3H), 7.28−7.1 (m, 9H), 6.97 (t, 3H), 6.75 (m, 3H).

$Na_{12}[Al_4L^2_4]$. A Schlenk flask was filled with methanol (75 mL) and degassed under nitrogen. Ligand H_6L^2 (150 mg, 0.19 mmol) and $Al(acac)_3$ (64 mg, 0.19 mol) were added. The suspended solids were sonicated for a few minutes to break up the aggregates. NaOH (32 mg, 0.57 mmol) was added as a small solid pellet, and the suspension slowly dissolved to form a light brownish-yellow solution. After the reaction was stirred for 15 h, the solvent was partially removed under vacuum until a precipitate began to appear. Degassed acetone (100 mL) was added to precipitate more beige solid. The amorphous solid was collected via filtration through a glass frit under a stream of nitrogen. Residual acetone was removed by blowing a stream of nitrogen through the solid residue on the frit for a few minutes and placing the product in a desiccator under vacuum. 95 mg (54%). ^{1}H NMR (500 MHz, D_2O) δ: 7.61 (bd, 24H), 7.42 (m, 36H), 7.27 (bd, 12H), 6.88 (bd, 12H), 6.62 (bt, 12H). ESI-MS spectrum of $Na_{12}[Al_4L^2_4]$ in MeOH. Three different charge states of the cluster are visible: 4− (approximate range m/z 800−25) m/z = 809 $\{Na_5H_3[Al_4L^2_4]\}^{4-}$ 5− (approximate range m/z 635−661) 639 $\{Na_3H_4[Al_4L^2_4]\}^{5-}$ and 6− (approximate range 520−540) 529 $\{Na_2H_4[Al_4L^2_4]\}^{6-}$.

$K(NMe_4)_{11}[Al_4L^2_4]$. 1,3,5-tris(4′-(2″,3″-dihydroxybenzamido)-phenyl)benzene (0.134 g, 0.176 mmol), $Al(acac)_3$ (0.057 g, 0.176 mmol), and NMe_4Br (0.095 g, 0.619 mmol) were suspended in degassed MeOH (30 mL), and the solution was degassed further for 10 min. KOH in methanol (0.5 M, 1.06 mL, 0.53 mmol) was added, and the reaction mixture was stirred at room temperature for 2 days. The yellow solution was filtered through Celite under nitrogen, and the clear yellow filtrate was evaporated to 1 mL. Acetone (5 mL) was added to precipitate a yellow solid, which was washed with acetone (100 mL) and dried under vacuum to yield $K(NMe_4)_{11}[Al_4L^2_4]$ as a yellow solid (0.158 g, 0.039 mmol, 89%). ^{1}H NMR (500 MHz, D_2O) δ: 14.65 (s, 12H), 7.68 (d, J = 8.5 Hz, 24H), 7.52 (s, 12H), 7.34 (d, J = 8.5 Hz, 24H), 6.97 (d, J = 7.8 Hz, 12H), 6.57 (d, J = 7.8 Hz, 12H), 6.42 (t, J = 7.8 Hz, 12H), 2.68 (s, 137H, NMe_4^+). High-Resolution ESI-MS: $\{H_6(NMe_4)_3[Al_4L^2_4]\}^{3-}$ (m/z = 1116.9923); $\{H_5(NMe_4)_3[Al_4L^2_4]\}^{4-}$ (m/z = 837.4946); $\{H_5(NMe_4)_2[Al_4L^2_4]\}^{5-}$ (m/z = 669.7847); $\{H_4(NMe_4)_3[Al_4L^2_4]\}^{5-}$ (m/z = 655.1735).

$K_{12}[Ga_4L^2_4]$. A Schlenk flask was filled with methanol (75 mL) and degassed under nitrogen. Ligand H_6L^2 (30 mg, 0.039 mmol) and $Ga(acac)_3$ (15 mg, 0.039 mmol) were added. The suspended solids were sonicated for a few minutes to break up the aggregates. KOH (0.237 mL, 0.117 mmol, 0.501 M in MeOH) was added and the suspension slowly dissolved to form a light brownish-yellow solution. After the reaction was stirred for 15 h, the solvent was partially removed under vacuum until a precipitate began to appear. Degassed acetone (100 mL) was added to precipitate a light beige solid. The amorphous solid was collected via filtration through a glass frit under a stream of nitrogen. Residual acetone was removed by blowing nitrogen through the residue on the frit for a few minutes and placing the solid in a desiccator under vacuum (Yield: 20 mg, 54%). ^{1}H NMR (400 MHz, MeOD-d_4) δ: 7.89 (bd, 24H), 7.33 (m, 36H), 7.14 (bd, 12H), 6.69 (bd, 12H), 6.36 (bt, 12H). ESI-MS spectrum of $K_{12}[Ga_4L^2_4]$ in MeOH. Three different charge states of the cluster are visible: 4− (approximate range m/z 850−900) m/z = 863 $\{K_4H_4[Ga_4L^2_4]\}^{4-}$ m/z = 869 $\{K_4NaH_3[Ga_4L^2_4]\}^{4-}$ m/z = 872 $\{K_5H_3[Ga_4L^2_4]\}^{4-}$ m/z = 878 $\{K_5NaH_2[Ga_4L^2_4]\}^{4-}$ m/z = 882 $\{K_6H_2[Ga_4L^2_4]\}^{4-}$ m/z = 891 $\{K_7H[Ga_4L^2_4]\}^{4-}$ m/z = 897 $\{K_7Na[Ga_4L^2_4]\}^{4-}$), 5− (approximate range m/z 675−705) m/z = 683 $\{K_3H_4[Ga_4L^2_4]\}^{5-}$ and 6− (approximate range m/z 560−580) m/z = 563 $\{K_2H_4[Ga_4L^2_4]\}^{6-}$.

$(NMe_4)_{12}[Ga_4L^2_4]$. 1,3,5-Tris(4′-(2″,3″-dihydroxybenzamido)-phenyl)benzene (0.147 g, 0.193 mmol), $Ga(acac)_3$ (0.071 g, 0.193 mmol), and NMe_4Br (0.095 g, 0.619 mmol) were suspended in degassed MeOH (20 mL), and the solution was degassed further for 10 min. KOH in methanol (0.5 M, 1.16 mL, 0.58 mmol) was added, and the reaction mixture was stirred at RT overnight. The yellow solution was filtered through Celite under nitrogen, and the clear yellow filtrate was evaporated to 1 mL. Acetone (5 mL) was added to precipitate a yellow solid, which was filtered and dried under vacuum to yield $(NMe_4)_{12}[Ga_4L^2_4]$ as a yellow solid (0.188 g, 0.045 mmol, 94%). ^{1}H NMR (500 MHz, D_2O) δ: 14.65 (s, 12H), 7.98 (d, J = 8.5 Hz, 24H), 7.56 (s, 12H), 7.40 (d, J = 8.5 Hz, 24H), 7.14 (d, J = 7.8 Hz, 12H), 6.71 (d, J = 7.8 Hz, 12H), 6.40 (t, J = 7.8 Hz, 12H), 3.00 (s, 140H, NMe_4^+). High-Resolution ESI-MS of selected peaks: $\{H_4(NMe_4)_5[Ga_4L^2_4]\}^{3-}$ (m/z = 1222.6182); $\{H_5(NMe_4)_4[Ga_4L^2_4]\}^{3-}$ (m/z = 1196.6056); $\{H_5(NMe_4)_3[Ga_4L^2_4]\}^{4-}$ (m/z = 880.1888); $\{H_3(NMe_4)_4[Ga_4L^2_4]\}^{5-}$ (m/z = 718.5673).

$(NMe_4)_{12}[In_4L^2_4]$. 1,3,5-Tris(4′-(2″,3″-dihydroxybenzamido)phenyl)benzene (0.107 g, 0.141 mmol), $In(acac)_3$ (0.059 g, 0.143 mmol), and NMe_4Br (0.071 g, 0.464 mmol) were suspended in degassed MeOH (30 mL), and the solution was degassed further for 10 min. KOH in methanol (0.5 M, 0.85 mL, 0.43 mmol) was added, and the reaction mixture was stirred at RT overnight. The yellow solution was filtered through Celite under nitrogen, and the clear yellow filtrate was evaporated to 1 mL. Acetone (5 mL) was added to deposit a yellow solid, which was dried at 45 °C under vacuum to yield $(NMe_4)_{12}[In_4L^2_4]$ (0.136 g, 0.031 mmol, 87%). ^{1}H NMR (500 MHz, D_2O) δ: 15.04 (s, 12H), 8.08 (d, J = 8.4 Hz,

24H), 7.56 (s, 12H), 7.40 (d, J = 8.4 Hz, 24H), 7.18 (d, J = 7.9 Hz, 12H), 6.75 (d, J = 7.9 Hz, 12H), 6.41 (t, J = 7.9 Hz, 12H), 2.95 (s, 145H, NMe_4^+).

$K_8[Ti_4L^2_4]$. A Schlenk flask was filled with methanol (75 mL) and degassed under nitrogen. Ligand $H_6\mathbf{L}^2$ (200 mg, 0.26 mmol) and $TiO(acac)_2$ (69 mg, 0.26 mmol) were added. The suspended solids were sonicated for a few minutes to break up the aggregates. K_2CO_3 (36 mg, 0.26 mmol) was added at once. After being stirred for 48 h, the dark reddish orange solution contained a small amount of solid material. The solid residue was removed by filtration, and the solution was concentrated to 2 mL. Degassed ether (100 mL) was added to precipitate a reddish-orange solid. The amorphous material was collected via filtration through a glass frit under a stream of nitrogen. Residual solvent was removed by blowing nitrogen through the residue on the frit for a few minutes and placing the solid in a desiccator under vacuum. Yield: 120 mg (54%). ^{1}H NMR (400 MHz, MeOD-d_4) δ: 12.70 (s, 12H), 7.95 (m, 24H), 7.34 (m, 48H), 6.63 (m, 24H). ESI-MS spectrum of $K_8[Ti_4\mathbf{L}^2_4]$ in MeOH. Three different charge states of the cluster are visible: 3− (approximate range m/z 1095−1125) 1108 $\{K_3H_2[Ti_4\mathbf{L}^2_4]\}^{3-}$, 4− (approximate range m/z 802−841) 803 $\{H_4[Ti_4\mathbf{L}^2_4]\}^{4-}$ and 5− (approximate range 642−667) 642 $\{H_3[Ti_4\mathbf{L}^2_4]\}^{5-}$. Other peaks within each charge state result from proton/potassium exchanges. High-Resolution ESI-MS: $\{K_4H_1[Ti_4\mathbf{L}^2_4]\}^{3-}$ (m/z = 1121.1187), $\{K_3H_2[Ti_4\mathbf{L}^2_4]\}^{3-}$ (m/z = 1108.4698), $\{K_1H_3[Ti_4\mathbf{L}^2_4]\}^{4-}$ (m/z = 812.1116), $\{H_3[Ti_4\mathbf{L}^2_4]\}^{5-}$ (m/z = 641.9044).

$(NMe_4)_8[Ti_4L^2_4]$. 1,3,5-Tris(4′-(2″,3″-dihydroxybenzamido)phenyl)benzene (0.118 g, 0.156 mmol), $Ti(O)(acac)_2{\cdot}H_2O$ (0.038 g, 0.147 mmol), K_2CO_3 (0.024 g, 0.172 mmol), and NMe_4Br (0.047 g, 0.306 mmol) were suspended in degassed MeOH (20 mL) and heated to reflux overnight, during which time an orange precipitate formed. The reaction mixture was cooled to room temperature and filtered through Celite under nitrogen. The clear orange filtrate was evaporated to 3 mL, and an orange solid was precipitated by addition of ether, which was filtered using a sintered funnel under nitrogen to yield $(NMe_4)_8[Ti_4\mathbf{L}^2_4]$ as an orange solid (0.115 g, 0.030 mmol, 82%). ^{1}H NMR (300 MHz, MeOD-d_4) δ: 12.86 (s, 12H), 8.03 (d, J = 8.2 Hz, 24H), 7.61 (s, 12H), 7.44 (d, J = 8.2, 24H), 7.36 (d, J = 7.5 Hz, 12H), 6.64 (t, J = 7.5 Hz, 12H), 6.59 (d, J = 7.5 Hz, 12H), 3.07 (s, 94 H, NMe_4^+). High-Resolution ESI-MS: $\{H_4(NMe_4)_1[Ti_4\mathbf{L}^2_4]\}^{3-}$ (m/z = 1094.8706), $\{H_3(NMe_4)_2[Ti_4\mathbf{L}^2_4]\}^{3-}$ (m/z = 1119.2422), $\{H_3(NMe_4)_1[Ti_4\mathbf{L}^2_4]\}^{4-}$ (m/z = 820.9095), $\{H_2(NMe_4)_1[Ti_4\mathbf{L}^2_4]\}^{5-}$ (m/z = 656.5146).

Acknowledgment. The authors thank Dr. Ulla N. Andersen (UC Berkeley Microanalytical Facility) for assistance and the Alexander-von-Humboldt Foundation for a fellowship to G.S. This work was supported by NSF Grant No. CHE-0317011.

Supporting Information Available: Additional molecular model figures, ESI-MS spectra, and a CD spectrum. This material is available free of charge via the Internet at http://pubs.acs.org.

IC0505145